Light and Mass Transport Computations Guide the Fabrication of 3D-Structured TiO_2 and Au/TiO_2 Aerogel Photocatalysts for Efficient Hydrogen Production in the Gas Phase

Rebber, Matthias; Sannemüller, Hendrik; Jaruszewski, Michael; Pfannkuche, Daniela; Urakawa, Atsushi; Koziej, Dorota

DOI
10.1021/acs.chemmater.2c03503

Publication date
2023

Document Version
Final published version

Published in
Chemistry of Materials

Citation (APA)
Rebber, M., Sannemüller, H., Jaruszewski, M., Pfannkuche, D., Urakawa, A., & Koziej, D. (2023). Light and Mass Transport Computations Guide the Fabrication of 3D-Structured TiO_2 and Au/TiO_2 Aerogel Photocatalysts for Efficient Hydrogen Production in the Gas Phase. *Chemistry of Materials*, *35*(10), 3849-3858. https://doi.org/10.1021/acs.chemmater.2c03503

CHEMISTRY OF MATERIALS

pubs.acs.org/cm

Article

Light and Mass Transport Computations Guide the Fabrication of 3D-Structured TiO_2 and Au/TiO_2 Aerogel Photocatalysts for Efficient Hydrogen Production in the Gas Phase

Matthias Rebber, Hendrik Sannemüller, Michael Jaruszewski, Daniela Pfannkuche, Atsushi Urakawa, and Dorota Koziej*

Cite This: *Chem. Mater.* 2023, 35, 3849−3858

Read Online

ACCESS | Metrics & More | Article Recommendations | Supporting Information

ABSTRACT: Efficient mass transfer and light utilization are essential for high photocatalytic production rates. Here, we present a hierarchical three-dimensional (3D)-printed aerogel photocatalyst that unites both aspects by taking inspiration from the light scattering in clouds during photochemical processes and from mass transfer in plants during photosynthesis. We combine the geometric freedom of additive manufacturing with computational fluid dynamics and Monte Carlo simulations to guide the implementation of a self-supported aerogel in a continuous gas flow reactor. Here, 3D microstructuring reduced the pressure drop of a monolithic aerogel by 5 orders of magnitude without compromising the gas permeation and the light-harvesting efficiency of the intrinsic nanoporous material. We match the macroscopic thickness with the ultraviolet (UV) light penetration depth and show that the 3D aerogel of 1.1 mm thickness improves photocatalytic hydrogen production rates relative to the nanoparticle powder by a factor of five from 1.3 to 6.6 μmol g^{-1} h^{-1} for TiO_2 and from 30.0 to 141.8 μmol g^{-1} h^{-1} for Au/TiO_2, respectively. Ultimately, our approach can be applied for other nanomaterials to boost the overall performance of a variety of photochemical processes and reactor designs.

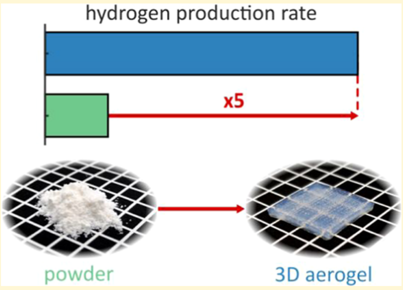

■ INTRODUCTION

Catalytic nanomaterials—especially for the photocatalytic conversion of solar energy into chemical fuels via CO_2 reduction or H_2 evolution—are considered as essential building blocks in the creation of a sustainable energy system.[1−3] While big progress on the material side was achieved by doping,[4,5] exposing reactive crystal facets,[6,7] loading cocatalysts,[4,6,8] or tuning selectivity in organic−inorganic hybrids,[9] technological implementation of photocatalytic nanomaterials is still pending.[10] One reason is that for an efficient photocatalyst, the nanoscopic material properties not only need to be optimized but also be well integrated into a macroscopic photoreactor where chemical and geometrical control at multiple length scales is of great importance.[11−13] In this regard, nature provides a blueprint for the synergy of elaborated structures and functional components to accelerate the solar energy conversion during photochemical processes.[14] Particularly, light harvesting via multiple scattering and efficient mass transfer in hierarchical structures are two main characteristics commonly found in nature.[15−19] Although catalyst designs advanced by replicating natural photocatalysts,[14,20−22] most efforts only focused on the functional imitation of a single characteristic by tuning geometrical aspects of the photoactive material either at the nano- and microscopic length scale in controlled aggregates[23−26] and biotemplated films[14] or at the macroscale by processing nanomaterials into monolithic aerogels.[27] Especially nanoparticle-based aerogels have huge potential as photocatalysts in the gas phase because they fully maintain the photocatalytic properties of the nanoscale building blocks in a macroscopic body composed of an interconnected nanoporous network and a translucent, light harvesting characteristic.[27,28]

Even though aerogels provide a high number of catalytic active sites based on their large specific surface area, bulk nanoporous materials generally suffer from poor gas permeability.[29−32] Thus, to unlock the full potential of an aerogel photocatalyst, the integration in a light and mass transport-optimized three-dimensional (3D) geometry with deterministic control of the nano-, micro-, and macroscopic length scales is essential.[12] A promising approach is the use of 3D printing, which successfully boosted mass transfer rates in heterogeneous catalysis and energy storage but so far has limited application for the production of solar fuels due to the opaque appearance of most photoactive inks which prevents a simultaneous interaction of light, reactant, and catalyst on the macroscopic scale of a 3D-printed object.[11,33−35,34,35]

Received: November 23, 2022
Revised: April 2, 2023
Published: May 8, 2023

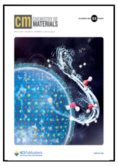

ACS Publications

https://doi.org/10.1021/acs.chemmater.2c03503

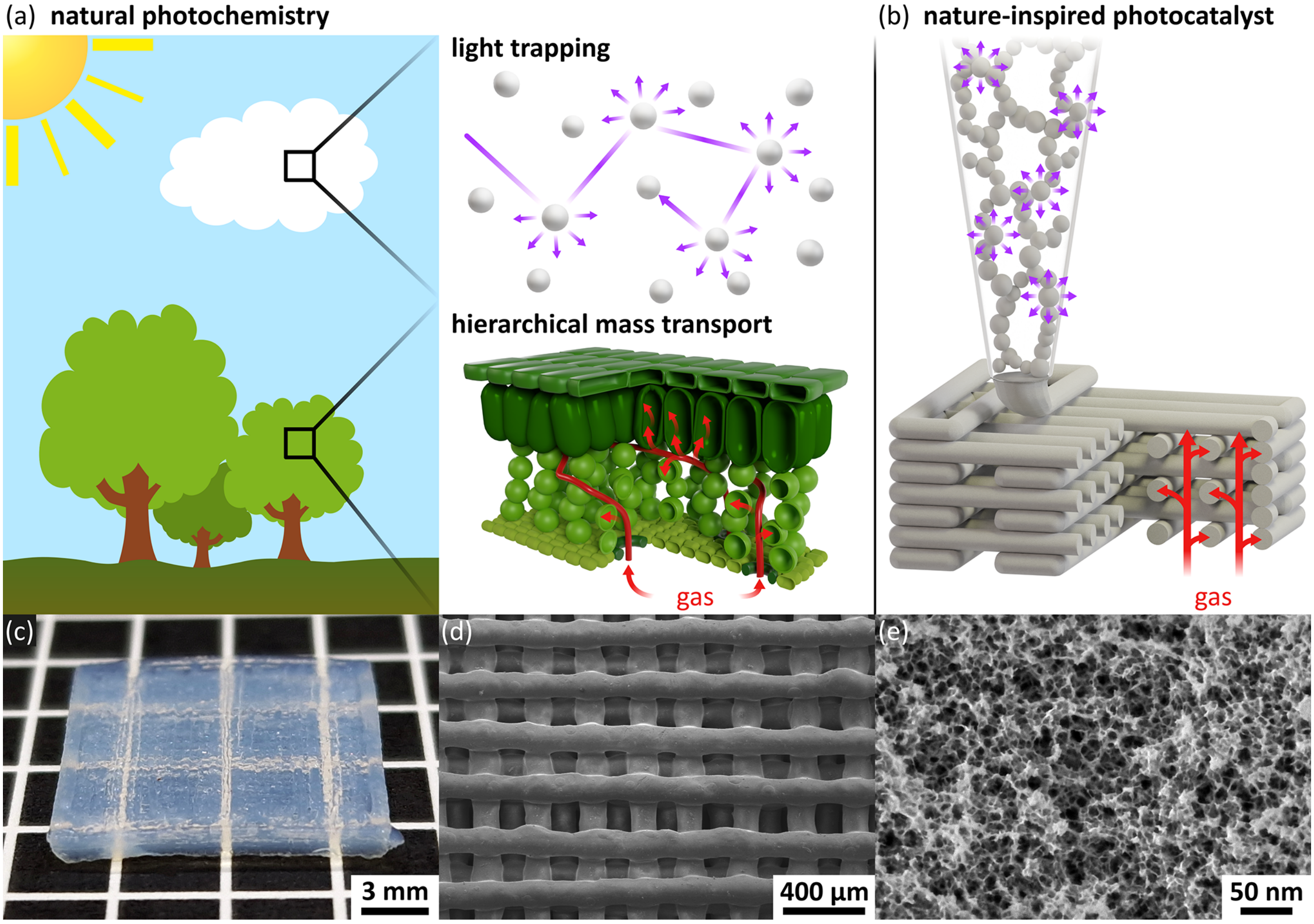

Figure 1. Photocatalyst with efficient light and mass transport. (a) Schematic illustration of two natural photochemical design principles: light trapping via scattering at water droplets in clouds and enhanced mass transport via diffusion in the hierarchical architecture of leaves. (b) Schematic showing that both design principles might be recreated in an artificial photocatalyst via 3D printing of gelled TiO_2 nanoinks. (c) Optical micrograph of the translucent, cloudy 3D-printed TiO_2 aerogel with lateral dimensions of 1.5 cm. (d, e) Scanning electron microscopy images reveal that the macroscopic aerogel consists of an array of nanoporous filaments with diameters of about 200 μm.

We overcome this limitation by 3D printing translucent TiO_2 nanoparticle-based aerogels, which combine a nature-inspired hierarchical mass transport and light trapping characteristic in a single photocatalyst. We utilize 3D printing, computational fluid dynamics, and Monte Carlo light transport simulations to systematically fabricate a photocatalyst geometry that optimally adapts the design of our continuous gas flow reactor. To this end, we evaluate the ultraviolet (UV) light utilization efficiency of various aerogel geometries, investigate the light penetration depth to eliminate poorly illuminated sections of the photocatalyst, and study the mass transfer characteristics to ensure an effortless infiltration with the gaseous reactants. We validate our approach by measuring the photocatalytic hydrogen evolution from a water/methanol-enriched gas stream and benchmark TiO_2 and Au/TiO_2 3D aerogels against the nanoparticle powder counterparts.

RESULTS AND DISCUSSION

We create nature-inspired photocatalyst geometries by 3D printing TiO_2 and Au/TiO_2 nanoparticle-based aerogels. Here, the 3D printing process replicates the microscopic mass transfer highways in hierarchically architectured leaves during photosynthesis,[19] whereas the gelled nanoparticles act as scattering centers and trap UV light similar to water droplets in clouds during atmospherical photochemical processes to enhance the absorption efficiency,[17] as illustrated in Figure 1a,b. Figure 1c−e shows an optical photograph and scanning electron microscopy images of a well-defined, 3D-printed TiO_2 aerogel that spans seven orders of magnitude, from the nanometer to centimeter length scale. The 3D-printed aerogel appears cloudy but translucent and features lateral dimensions of 1.5 cm and a thickness of 2 mm. The filaments have a diameter of about 200 μm and consist of a nanoporous, finely branched network of nanoparticles that formed during the ink gelation process. Although a cloudy appearance and a hierarchical architecture can readily be imitated with our 3D printing process, we need to go one step further and engineer the macro- and microscopic geometry toward the highest photocatalytic efficiency. To this end, we utilize different 3D microstructures and benchmark their mass and light transport characteristics against an unstructured aerogel.

Figure 2a,b shows 3D renderings of a simple cubic (sc)-structured and face center cubic (fcc)-structured aerogel, respectively. For both geometries, each layer consists of an array of parallel filaments where the center-to-center spacing is twice the filament diameter, and alternating layers are orientated 90° to each other. Depending on the type of structuring, consecutive layers of the same orientation are either aligned to

https://doi.org/10.1021/acs.chemmater.2c03503
Chem. Mater. 2023, 35, 3849−3858

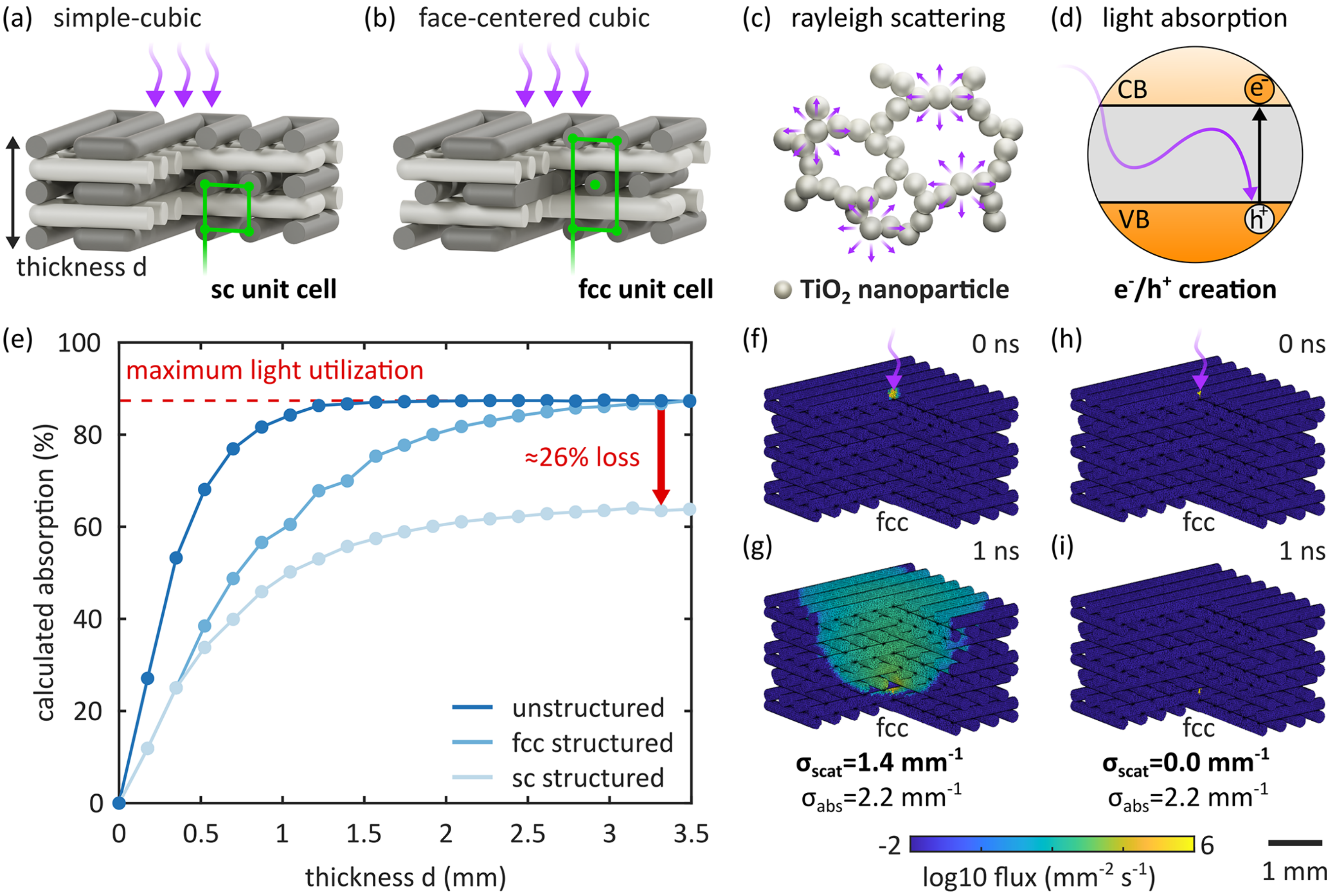

Figure 2. Light transport through a 3D-printed TiO_2 aerogel is defined by light−matter interaction from the macro- to the nanoscale. Schematic illustration of the macroscopic 3D-printed aerogel where the microscopic filaments are arranged in (a) a simple-cubic (sc) or (b) a face-centered cubic (fcc) unit cell. Within the nanoporous TiO_2 network, (c) light scattering and (d) light absorption processes take place. (e) Calculated absorption for unstructured, fcc-structured, and sc-structured TiO_2 aerogel microlattices with thicknesses in a range of 0−3.5 mm according to 3D mesh-based Monte Carlo simulations. Time-resolved flux in an fcc-structured aerogel after 0 and 1 ns obtained by 3D mesh-based Monte Carlo simulations (f, g) in the presence and (h, i) absence of scattering, respectively. For both simulations, photons with a wavelength of 375 nm are launched at the top of the microlattice as a collimated, infinitely thin pencil beam.

yield an sc-geometry or shifted by one filament diameter for an fcc-geometry. Generally, 3D structuring creates aerogel/air interfaces that enable refraction and specular reflection of light upon transitioning from one medium to the other. However, we calculate in the Supporting Information that refraction and specular reflection can be neglected due to the low refractive index of the aerogel. Thus, the transparency and light propagation in the 3D-structured aerogel is purely defined by the light−matter interaction within the nanoporous material and is not affected by the type of microstructure. We extract the scattering and absorption coefficients of the TiO_2 aerogel from experimental UV−visible (UV−vis) transmission and reflection data by solving the inverse problem of the radiative transfer equation, as described in Section SI1 of the Supporting Information.[36] Here, we identify Rayleigh scattering (Figure 2c) and electron excitation from the valance to the conduction band by UV light (Figure 2d) as the main light redirection and absorption mechanisms in the TiO_2 aerogel, respectively. While Rayleigh scattering is unique for the nanoporous structure of the translucent aerogel, electron excitation due to UV light absorption, exists for any TiO_2-based material. Further, we combine the derived optical coefficients of the aerogel with the Monte Carlo method to calculate the number of absorbed photons for unstructured, sc-structured, and fcc-structured samples with thicknesses in the range of 0−3.5 mm, as shown in Figure 2e. We see that the unstructured and fcc-structured aerogels reach similar absorption values with increasing sample thickness, whereas the maximum absorption for the sc unit cell is about 26% lower. The drastically lower light utilization of the sc structure is a result of the filament stacking sequence, which allows light to pass the aerogel without being absorbed. In the fcc structure, the consecutive layers of the same orientation are shifted by one filament diameter, which obstructs the formation of a direct line of sight. Moreover, we performed time-resolved Monte Carlo simulations for a scattering and nonscattering sample to reveal the impact of the Rayleigh scattering process on the light distribution in the fcc structures. In the absence of any scattering, the infinitely thin pencil beam, which is launched at the top of the fcc-structured aerogel, just passes through the sample without any redirection of the photon path (Figure 2h,i). In contrast, Rayleigh scattering drastically spreads the incoming light and enables a more uniform light distribution on a macroscopic scale (Figure 2f,g). When comparing the flux distribution after 1 ns in Figure 2g,i, a longer residence time of the photons becomes apparent in the presence of Rayleigh scattering. Thus, light is trapped in the aerogel in a similar fashion as in clouds during natural photochemical processes, which enhances the probability of absorption.

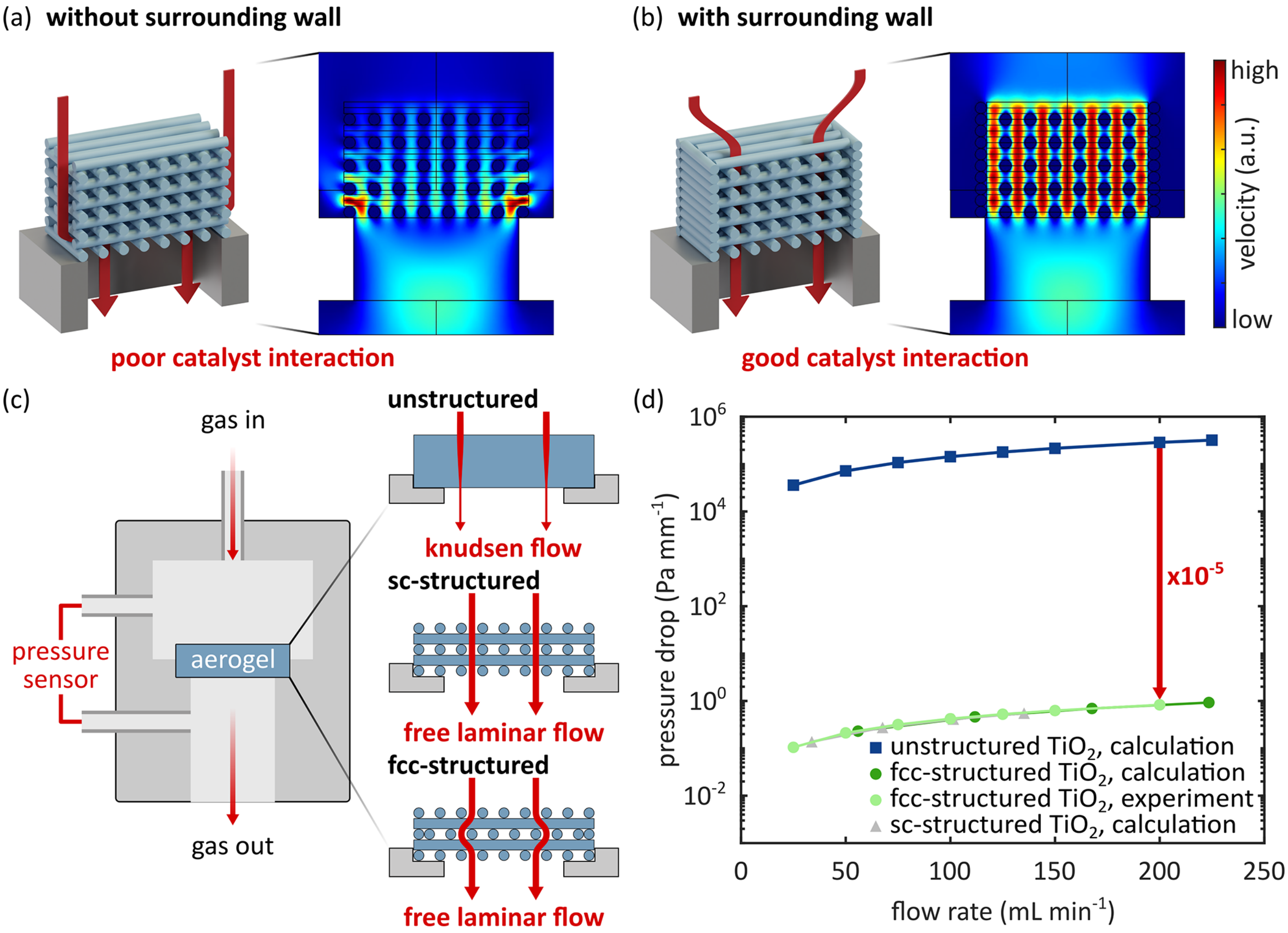

Figure 3. Effect of 3D structuring on the mass transport characteristic of TiO_2 nanoparticle-based aerogels. Simulated velocity profiles of an sc-structured aerogel (a) without and (b) with a surrounding wall indicate that the geometry needs to be enclosed for a good interaction of the gas stream with the catalyst. (c) Schematic drawing of a custom flow-through reactor that was utilized to evaluate the pressure drop of an unstructured and structured aerogel. For an unstructured and 3D-structured aerogel, mass transport is dominated by Knudsen flow through the nanoporous medium and free, continuum flow through the microscopic channels of the 3D architecture, respectively. (d) Measured and calculated pressure drops of unstructured and 3D-structured aerogels for flow rates in a range of 25−225 mL min^{-1}.

Photocatalytic processes require not only effective utilization of the incident light but also efficient mass transport to the illuminated catalyst surface. To this end, we take advantage of a leaf-type hierarchical architecture in sc- and fcc-structured aerogels, where the gas enters the macroscopic object through microchannels and then distributes into the nanoporous filaments to perform photocatalytic reactions. Computational fluid dynamics simulations in Figure 3a,b reveal that such a hierarchical flow characteristic can only be achieved by surrounding the microstructured aerogel geometry with continuous walls, which can be easily added during the 3D printing process. Moreover, only with surrounding walls, a pronounced interaction with the stronger illuminated section at the top of the photocatalyst becomes feasible. We evaluate the gas transport properties of sc-, fcc-, and unstructured aerogels in a custom flow-through reactor illustrated in Figure 3c by measuring the pressure drop of nitrogen gas in the flow range of 25−225 mL min^{-1}. In Figure 3d, we show that the fcc-structured aerogel exhibits a pressure drop of less than 1 Pa mm^{-1} (dark green dots), which agrees well with the predicted pressure drop obtained by computational fluid dynamics simulations (light green dots). Calculations of an sc-structured aerogel forecast a similar pressure drop as for the fcc-pattern due to the similar channel dimensions (gray triangles). In contrast, an unstructured sample, which represents the geometry of a conventionally casted aerogel, exceeds the upper pressure limit of 125 Pa for the used pressure sensor, and calculations following Darcy's law predict a pressure drop of more than 10^5 Pa mm^{-1} (blue squares). The reason for the five orders of magnitude higher pressure drop for the unstructured aerogel relies on the mean free path of the nitrogen gas molecule of about 59 nm, which is higher than the aerogel's average pore size of 20 nm (Figure SI1b).[37] Thus, the transport is dominated by molecule−wall interactions, and high pressure differences are needed to squeeze the gas through the nanoporous network. In contrast, the sc- and fcc-structured sample offers 400 channels per cm^2 with dimensions of about 0.2 mm, which allows the gas molecules to flow freely and laminar through the 3D geometry, as derived in Section SI3 of the Supporting Information. Nevertheless, reducing the pressure drop by 3D structuring does not necessarily correlate with an improved transport of reactants to the catalyst surface. In fact, the high pressure drop for an unstructured aerogel has the advantage that the gas is uniformly squeezed through the nanoporous network as long as the resulting mechanical load does not lead to the uncontrolled formation of cracks and gas channeling.[12] In contrast, for a 3D-

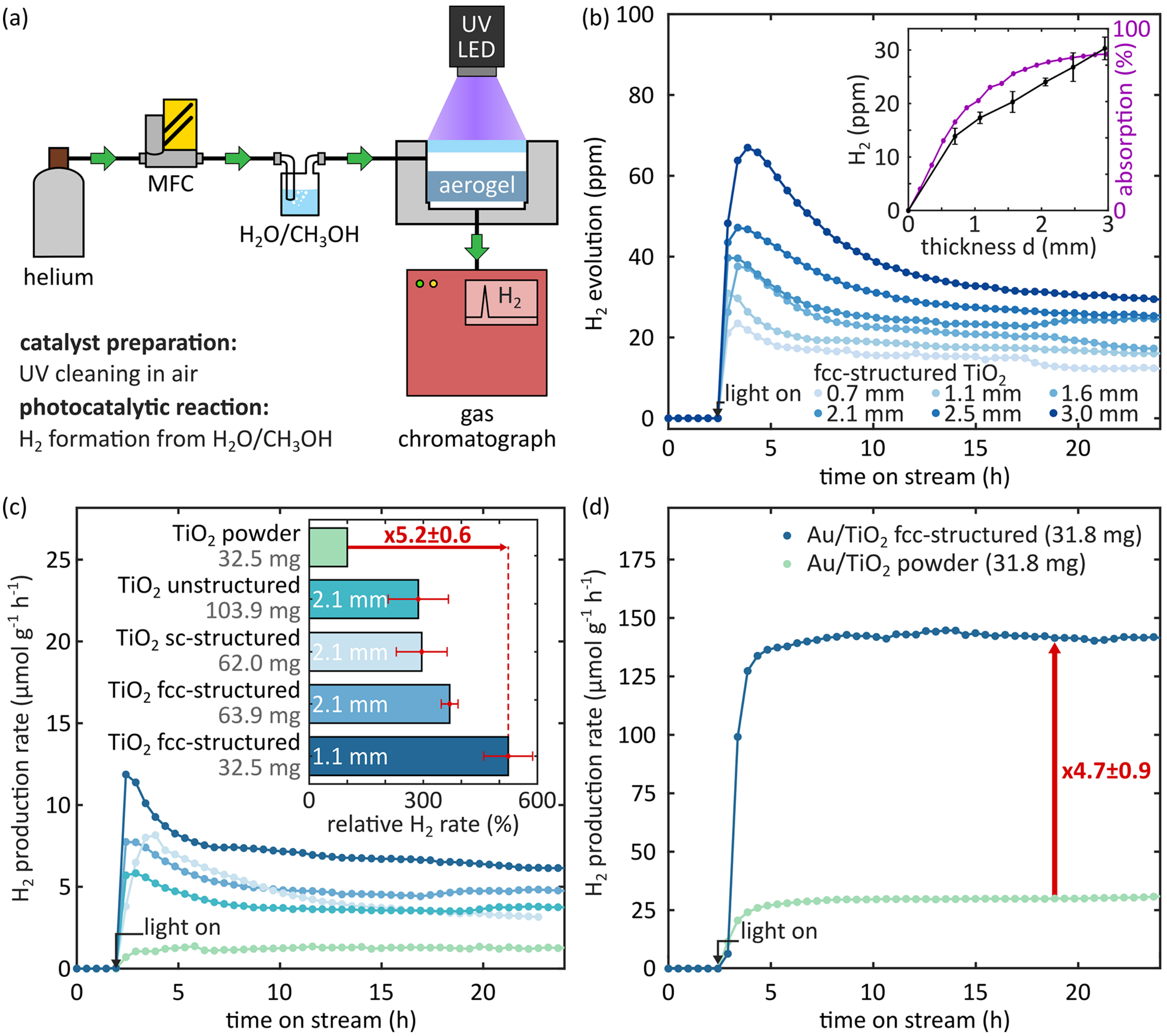

Figure 4. Effect of 3D structuring on photocatalytic hydrogen evolution in the gas phase. (a) Schematic representation of the custom-made continuous gas flow reactor. Before each photocatalytic measurement, the samples are illuminated with UV light in a steady air stream to remove any organic residue from the catalyst surface. For the photocatalytic measurement, a helium gas stream is regulated with a mass flow controller and saturated with water and methanol vapor. The gas stream enters the reactor at the top and passes through the sample while being illuminated with a UV LED. Following that, the gas stream containing reactants and products of the photocatalytic reaction is directed to a gas chromatograph for the quantification of the evolved hydrogen. (b) Mean absolute hydrogen evolution vs time for fcc-structured TiO_2 aerogels with thicknesses in the range of 0.7−3.0 mm. The photocatalyst features a transient activity, which declines within a couple of hours into a steady-state value. The inset shows the average and standard deviation of the steady-state region and the calculated light absorption from 3D mesh-based Monte Carlo simulations plotted vs the sample thickness. (c) Mass-normalized hydrogen production rate vs time for TiO_2 powder, an unstructured TiO_2 aerogel of 2.1 mm thickness, and fcc-structured TiO_2 aerogels of 2.1 and 1.1 mm thickness, respectively. The inset shows the hydrogen production rate relative to TiO_2 powder. (d) Mass-normalized hydrogen production rate vs time for an fcc-structured Au/TiO_2 aerogel of 1.1 mm thickness and Au/TiO_2 powder. All samples feature lateral dimensions of 1.5 cm to obtain a similarly illuminated surface area.

structured aerogel, reactants are no longer actively forced through the nanoporous network but need to diffuse from the microchannels into the aerogel to be converted during the photocatalytic process. In this case, the conversion might be limited by the supply of reactants if the reaction proceeds much faster than the diffusion to the center of the aerogel filament. In Section SI2 of the Supporting Information, we conclude that for a filament diameter of 200 μm, no internal mass transfer limitations are present and that the whole catalyst participates in the reaction. Thus, the key attributes of 3D-structured aerogels in terms of mass transport are minimized energy consumption and reliable operation due to the drastically lower pressure drop without compromising the permeation of the aerogel with reactants. Moreover, we learned that the type of structuring is not as relevant for the flow resistance as for the light utilization as long as some type of structuring is present.

Combining the insights from the photon and mass transport simulation reveals that the fcc structure is most promising for a photocatalytic application, since we achieve similar levels of light utilization as for an unstructured aerogel with a five order of magnitude lower resistance to gas flow. With a photon and mass transport-optimized microstructure in place, we can now compare the performance of fcc-, sc-, and unstructured aerogels against nanoparticle powder for the hydrogen formation from a helium gas stream saturated with a water/methanol mixture, as shown in Figure 4a. Methanol is a more efficient hole scavenger than water and facilitates hydrogen formation (see Figure SI2).[8,38] The photoreactor reflects the aspect ratio of the 3D-printed aerogels and is designed in such a way that the gas stream and photons penetrate the sample from the top. The evolved hydrogen is detected via gas chromatography every 29 min. Although the synthesis of TiO_2 nanoparticles is considered as ligand-free,[39] solvents are involved during the processing of the 3D-printed aerogels that remain attached to the surface of the nanoparticles after supercritical drying. These organic species may interfere with the photocatalytic hydrogen production process, where their decomposition during UV illumination results in misleading amounts of detected hydrogen or block catalytic active sites.[40] We apply a UV pretreatment in air prior to each measurement, during which an online analysis via gas chromatography reveals that organic species decompose within 15 h of illumination (Figure SI3). Moreover, performing the catalytic reaction in the absence of water and methanol subsequent to UV cleaning fails to produce any hydrogen. Thus, we conclude that the UV cleaning process effectively removes organic residues from the catalyst surface and that the hydrogen formation stems from the photocatalytic conversion of methanol and water on the TiO_2 aerogel. In the presence of water/methanol, we observe a strong formation of hydrogen, which declines within a couple of hours before reaching a steady-state value (Figure 4b). Such a transient activity is a common effect for TiO_2 photocatalysts in the gas phase and is generally attributed to the formation of intermediate surface species, which are partly occupying the active sites and originate from the oxidation of methanol.[38,41−45] We observe that the conversion of methanol yields carbon dioxide and methyl formate (see Figure SI4).

The transient activity recovers after performing a second UV cleaning process, as shown in Figure SI5. We take the average of the steady-state values to evaluate the absolute amount of evolved hydrogen for fcc-structured TiO_2 aerogels with thicknesses in the range of 0.7−3.0 mm. In the inset of Figure 4b, we see that the steady-state hydrogen evolution of the fcc-structured TiO_2 aerogel reaches 30 ppm for a thickness of 3.0 mm and follows a similar thickness dependence as the calculated light absorption from 3D mesh-based Monte Carlo simulations. Compared to an unstructured aerogel with similar light absorption, the absolute amount of evolved hydrogen for the fcc-structured aerogel is almost identical (Figure SI6), which indicates that the permeation of the 3D-structured aerogel with reactants is not compromised despite the diffusive mass transport through the nanoporous filament with a diameter of 200 μm. Besides, the hydrogen production rate is independent of the flow rate in a range of 1.25−20 mL min^{-1}, which indicates that the conversion is not limited by the supply of reactants (Figure SI7). Nevertheless, for other photocatalytic processes or materials with a higher conversion rate, a smaller filament diameter and channel dimension might be needed to prevent any diffusion limitation.

Even though a thicker aerogel results in a higher absolute amount of evolved hydrogen (Figure 4b), the increase diminishes due to the decreasing light intensity. Therefore, tripling the thickness of an fcc-structured TiO_2 aerogel from 1 to 3 mm only rises the absolute amount of hydrogen by a factor of about 1.8. To enhance the utilization of the photocatalyst, an adjustment of the thickness for the most effective use of the incident light is needed. We describe the effective use of the photocatalyst by calculating a mass-normalized hydrogen production rate for fcc-, sc-, and unstructured aerogels and a nanoparticle powder, which is still one of the most employed approaches to benchmark a photocatalyst.[12] We present the mass-normalized hydrogen production rates in Figure 4c. For identical outer dimensions and a thickness of 2.1 mm, the fcc-structured TiO_2 sample shows the highest rate of all aerogel microstructures. We attribute the increase relative to the unstructured aerogel to the improved illumination along the catalyst thickness, which results from the added porosity of the microchannels, and the increase relative to the sc-structured aerogel to the higher light utilization of the fcc structure, respectively (Figure 2e). Further, by varying the number of printed layers, we can match the thickness of the fcc-structured aerogel to the light intensity distribution. In this way, decreasing the thickness from 2.1 to 1.1 mm enhances the hydrogen production rate by 41%, and we achieve a total improvement by a factor of 2.3 relative to the unstructured TiO_2 aerogel. Compared to the same amount of a TiO_2 nanoparticle powder, the hydrogen production rate of the 1.1 mm thick fcc-structured aerogel is 5.2 times higher, which results from combining an efficient illumination with an about 3.2 times higher specific surface area of the nanoporous solid (Figure SI1).

Due to the modular ink design principle, pristine TiO_2 gels can also be loaded with 0.9 wt % Au nanoparticles of 30 to 40 nm (Figure SI8) without compromising the specific surface area and pore size distribution of the final aerogel (Figure SI1c,d). We show the hydrogen production rate of an fcc-structured Au/TiO_2 aerogel of 1.1 mm thickness and Au/TiO_2 powder in Figure 4d. Generally, we observe that the hydrogen production rates of Au-decorated TiO_2 feature no transient activity and are about 20 times higher than pure TiO_2 due to less electron−hole recombinations and a reduced activation barrier for hydrogen formation.[8,46,47] Apart from the material-specific improvement, the mass-normalized hydrogen production rate of the fcc-structured Au/TiO_2 aerogel again rises nearly fivefold by a factor of 4.7. We attribute the slightly lower enhancement relative to the factor of 5.2 for pure TiO_2 to the reduced light penetration depth owing to the additional light absorption of Au nanoparticles. The similarity of both values indicates that our microstructuring approach is a universal, geometric tool and that similar improvements can be expected for other photocatalytic materials than TiO_2 or Au/TiO_2 when processed in the form of an fcc-structured aerogel of comparable surface area. Nevertheless, for other materials with drastically different optical properties, an adjustment of the 3D aerogel thickness is needed to compensate for the varying light penetration depths.

CONCLUSIONS

We provide a fundamental understanding of light and mass transport in 3D-printed aerogel structures to enhance the photocatalytic efficiency in a continuous gas flow reactor. By computational fluid dynamics and Monte Carlo simulations, we propose an fcc unit cell as an ideal photocatalyst microstructure since it combines the light utilization of an unstructured aerogel with a five order of magnitude lower resistance to gas flow. We take the hydrogen evolution from a water/methanol-saturated gas stream as an example and show that filament diameters of 200 μm are sufficient to ensure a full permeation of the 3D-structured aerogel with reactants. Moreover, 3D printing permits a most effective illumination of the catalyst by tuning the macroscopic thickness toward the light penetration depth. In this way, the mass-normalized hydrogen evolution rate for 3D TiO_2 and Au/TiO_2 aerogels rises by a factor of 5.2 and 4.7 in respect to the nanoparticle powder counterparts, respectively. We believe that a similar 5-fold improvement can be achieved for other nanomaterials as long as the 3D-structured aerogel possesses a comparable surface area and a thickness tuned to the light penetration depth. Ultimately, the combination of 3D printing with a computer-aided design scheme provides a great platform for engineers and scientists to design, optimize, and implement innovative aerogel photocatalysts for a variety of photochemical processes.

EXPERIMENTAL SECTION

Chemicals. Acetonitrile (99.95%), diethyl ether (≥99.9%), and ethanol (EtOH, anhydrous, ≥99.97%) were purchased from VWR. Ammonium hydroxide solution (28.0−30.0% NH_3 basis), benzyl alcohol (anhydrous, 99.8%), gold(III) chloride trihydrate (>99.9%), poly(methyl methacrylate) (PMMA, average M_w = 120,000), poly(vinylpyrrolidone) (PVP, average M_w = 40,000), sodium borohydride ($NaBH_4$, 99%), and titanium(IV) tetrachloride ($TiCl_4$, 99.9% trace metal basis) were purchased from Sigma-Aldrich. n-heptane (95%) was purchased from Alfa Aesar. Liquid CO_2 and helium (purity 5.0) were purchased from Westfalen. Hydrogen (purity 5.0) was purchased from Linde. Nitrogen (purity 6.0) and synthetic air (hydrocarbon free) were purchased from SOL Deutschland GmbH. Calibration gases for quantification of hydrogen were purchased from Air Liquide Deutschland GmbH. All chemicals were used as received without further purification.

TiO_2 Synthesis. TiO_2 nanoparticle synthesis was adapted from a previously published protocol.[39] In an argon-filled glovebox, 40 mL of benzyl alcohol was added to a 100 mL round-bottom flask. Next, the flask was closed with a stopper and transferred to an oil bath set to 80 °C while stirring and keeping the flask closed. In the meantime, 2 mL of $TiCl_4$ was dropwise added to a 50 mL round-bottom flask containing 10 mL of EtOH while stirring. After heating the benzyl alcohol for 10 min, the transparent yellow $TiCl_4$/EtOH solution was swiftly added. The obtained solution was heated for 24 h while keeping the flask open. After that, the flask was immersed into an ambient water bath to quench the reaction. Next, the suspension was washed with diethyl ether (≈4.7 mL of diethylether per 1 mL of dispersion) by three dispersion−centrifugation cycles (1160 RCF, 5 min, room temperature, Universal 320 centrifuge, Andreas Hettich GmbH & Co. KG). Afterward, the supernatant was removed by decantation, and the vial was loosely covered with a cap for slow evaporation of the remaining solvent. Finally, the dried precipitate was mortared to yield 1 g of a white powder.

Ink Formulation. Inks for 3D printing were formulated according to a previously reported procedure but additionally filtered with a 0.2 μm nylon syringe filter (KC92.1, Carl Roth) prior to gelation.[48] TiO_2 inks were loaded with Au by adapting a previously published protocol.[49] $HAuCl_4$ (16 mM) and $NaBH_4$ (132 mM) stock solutions were prepared by dissolving the salts in acetonitrile, which was degassed beforehand by purging with nitrogen gas for 15 min. Next, 1 mL of an aqueous, degassed TiO_2 dispersion (241 mg mL^{-1}) and 384 μL of the $HAuCl_4$ stock solution were added to a vial. After 1 min, 116 μL of freshly prepared $NaBH_4$ stock solution was quickly injected to the vigorously stirred solution. After 30 min of stirring at room temperature, the inks were stored in a refrigerator prior to gelation. For gelation, we applied the same procedure as described above for neat TiO_2 inks.

3D Printing and Aerogel Fabrication. For 3D printing, tapered dispensing tips with an inner diameter of 250 μm from Vieweg GmbH were used. The 3D printing process is described in more detail in a previously published protocol.[48] After 3D printing, the water/acetonitrile mixture contained in the wet gel was gradually exchanged for ethanol. For this, the samples were immersed for at least 1 day into solvent mixtures with different volume ratios: water/acetonitrile = 1.4:1, 50:50, 40:60, 30:70, 20:80, 10:90, 0:100, 0:100, followed by acetonitrile/ethanol = 50:50, 0:100, 0:100. In a final step, the wet gels were soaked in liquid carbon dioxide and supercritically dried in a Quorum E3100 to yield aerogels.

Photocatalytic Measurements. The photocatalytic hydrogen evolution from aerogels and nanoparticle powders was analyzed using a custom-made continuous gas flow reactor at room temperature and atmospheric pressure, as shown in Figures 4a and SI9. All aerogels were obtained following the scheme as described in the 3D Printing and Aerogel Fabrication Section above. The TiO_2 powder was obtained by ambient drying of a TiO_2 nanoparticle precipitate after washing, as described in the TiO_2 Synthesis Section. The Au/TiO_2 powder was obtained by precipitating the ungelled Au/TiO_2 ink (see Ink Formulation Section) with an excess of acetonitrile, followed by centrifugation, decantation, and ambient drying. The weights, absolute amounts of hydrogen, and the mass-normalized hydrogen production rates of the catalysts are listed in Table SI2. The self-supporting aerogels were fixed inside the reactor with grease to avoid bypass of the gas stream. The loose powder was spread on a filter paper, which was sealed in the same way as the aerogel. The viewport was sealed with an FPM75 O-ring. All gas connections were made with stainless steel tubing, and the gas flows were adjusted using mass flow controllers (MFC, Bronkhorst). The outlet of the reactor was connected to a gas chromatograph (Agilent 8860) equipped with a Deans switch, which directs the eluent from the PoraPLOT U (25 m × 0.32 mm × 10 μm) column either to a series of thermal conductivity and flame ionization detector or to a series of a HP-Plot 5A (30 m × 0.32 mm × 25 μm) column and a helium ionization detector. The hydrogen signal was calibrated with commercial calibration gases containing defined amounts of hydrogen. The gas chromatograph enables sample acquisition every 29 min. Before each measurement, the samples were UV-cleaned in the reactor for 24 h at room temperature in a continuous flow of synthetic air at a flow rate of 5 mL min^{-1} and UV illumination with a 200 W Hg/Xe arc lamp (66984-200HX-r1, Newport) equipped with a water filter (61945, Newport) to remove IR light from the light source. Gas chromatograph measurements were performed to monitor the cleaning process. IR spectra and results of CHN elemental analysis of UV-cleaned TiO_2 aerogel and powder are shown in Figure SI10 and Table SI3, respectively. After UV cleaning, helium was bubbled through a custom-made stainless steel chamber filled with water and methanol (1:1 v/v) to enrich the gas stream with water and methanol vapor. Before light illumination, the flow rate was set to 20 mL min^{-1} to remove oxygen residues in the tubing and reactor. Next, the flow rate was decreased to 5 mL min^{-1}, and the sample was illuminated with a high-power LED (M375L4, Thorlabs) with an emission peak at 375 nm. The output of the LED was collimated with an aspheric condenser lens (ACL2520U-DG6-A, Thorlabs) and illuminated the whole sample area. The output power was measured with a photodiode power sensor (S120VC, Thorlabs). For this, the same distance between the light source and sensor as between the light source and sample was used. For the photocatalytic experiments, the power of the LED was set to 116 mWcm^{-2} and was controlled via a custom-made electronic circuit consisting of a power supply, an LED driver (LDD-1500H, Mean Well), and an Arduino Uno. Control experiments were carried out with an empty reactor in a water/methanol-saturated helium gas stream and with a TiO_2 aerogel sample inside the reactor in a dry helium gas stream, and no hydrogen evolution was observed.

Computational Modeling. For photon transport in 3D-structured and unstructured geometries, tetrahedral meshes were generated using the MATLAB-based program Iso2mesh.[50] For computing reasons, the mesh represents a small section of the periodic geometry. In detail, the number of filaments per layer was reduced from 39 to 8 for the structured samples. Moreover, the dimensions of the unstructured geometry were scaled to achieve a similar optical thickness in a lateral direction than for the structured geometries. The generated meshes were used to perform 3D Monte Carlo light transport simulations with

MMCLAB.[51] The optical parameters were extracted from solving the inverse problem of the radiative transfer equation and UV−vis integrating sphere measurements, as described in Section SI1 of the Supporting Information. The light source was either a pencil beam or a circular disk source with a diameter of twice the filament diameter. For each calculation, at least 50,000 photons were used. We verified mesh independence by calculating the absorption of a 3.5 mm thick fcc-structured aerogel for three different mesh sizes of 5.1, 8.7, and 14 million elements. The calculated absorption varied by less than 0.1%, and the mesh featured a mean Joe-Liu mesh quality metric of 0.8.[52] Computational fluid dynamics simulations were performed with the "Free and Porous Media Flow" Interface of COMSOL Multiphysics software (COMSOL 5.4). Computations were performed on a computing cluster (4xAMD EPYC 7302 processors, available RAM: 2060.17GB). Mesh convergence was verified for three different mesh sizes of 2.1, 2.4, and 5.2 million elements, respectively. The pressure drop calculations for the three meshes varied by less than 1.3%. For a more detailed description of the simulations, we refer to Section SI3 in the Supporting Information.

Characterization. The dimensions of the sample were determined from optical micrographs, and the mass was measured using a microbalance (LA 254i, VWR). The density of the samples was calculated from the measured mass and dimensions. Scanning electron microscopy images were taken with a Regulus 8220 (Hitachi High Technologies Corp., Japan). Nitrogen physisorption measurements are shown in Figure SI1 and were performed at 77 K with a Quantachrome Autosorb 6-MP (Anton Paar QuantaTec Inc.). The specific surface area and pore size were determined via the Brunauer−Emmet−Teller (BET) method and density functional theory (DFT) analysis, respectively. For DFT analysis, a Non Local DFT (NLDFT) calculation model for nitrogen at 77 K using the equilibrium branch was applied, and cylindrical pores in silica were assumed. Prior to measurement, samples were degassed at 100 °C for 24 h. Transmission electron microscopy (TEM) and scanning transmission electron microscopy (STEM) images were taken with a JEM 1011 (JEOL Ltd., Japan) and JEM-2200FS (JEOL Ltd., Japan), respectively. TEM and STEM images of an Au/TiO_2 aerogel are shown in Figure SI8. The Au loading of the Au/TiO_2 aerogels was determined by inductively coupled plasma mass spectrometry (ICP-MS, Agilent 7700 series). Fourier transform infrared spectra were recorded on a Bruker ALPHA II spectrometer equipped with an attenuated total reflection module. Carbon, hydrogen, nitrogen (CHN) elemental analysis was performed on a Vario EL III (Elementar Analysensysteme GmbH). Powder X-ray diffraction measurements are shown in Figure SI11 and were performed on a Bruker D8 Discovery using Cu Kα X-ray radiation. UV−vis spectra were recorded using an Agilent Cary 5000 spectrophotometer equipped with a 150 mm integrating sphere. Pressure drop experiments were performed in a custom-designed flow cell, as shown in Figure 4a. The pressure drop was measured with a differential pressure sensor (SDP810-125 Pa, Sensirion) with a detection range of 0 to 125 Pa. The edges of the 3D-printed aerogel sample were sealed with grease, and flow rates between 0 and 200 mL min^{-1} of nitrogen gas were used.

■ ASSOCIATED CONTENT

Data Availability Statement

The data that support the findings of this study are openly available in the zenodo repository at http://doi.org/10.5281/zenodo.7018488.[53]

Supporting Information

The Supporting Information is available free of charge at https://pubs.acs.org/doi/10.1021/acs.chemmater.2c03503.

Nitrogen isotherms, surface areas, and pore size distributions of TiO_2 and Au/TiO_2 aerogels; gas chromatography data of the UV cleaning procedure, of two consecutive photocatalytic runs for a fcc TiO_2 aerogel, of an fcc and unstructured TiO_2 aerogel of similar thickness, and of photocatalytic runs at varying flow rate; insights on the reaction mechanism based on gas chromatograms; technical drawing, photograph, and experimental conditions of the custom-made gas flow reactor; weight, absolute amount of evolved hydrogen, and calculated hydrogen production rate of various TiO_2 and Au/TiO_2 photocatalysts; attenuated total reflection infrared spectra of TiO_2 nanoparticle powder and aerogel after UV cleaning; results of CHN elemental analysis; data processing for hydrogen production rates of TiO_2 powder; XRD pattern of TiO_2 nanoparticles; calculation of the apparent quantum efficiency; optical characterization of TiO_2 aerogels; mass transport considerations; and details on computational fluid dynamics simulation (PDF)

■ AUTHOR INFORMATION

Corresponding Author

Dorota Koziej − *Institute for Nanostructure and Solid State Physics, Center for Hybrid Nanostructures (CHyN), 22761 Hamburg, Germany; The Hamburg Centre for Ultrafast Imaging, 22761 Hamburg, Germany;* orcid.org/0000-0002-9064-2642; Email: dorota.koziej@uni-hamburg.de

Authors

Matthias Rebber − *Institute for Nanostructure and Solid State Physics, Center for Hybrid Nanostructures (CHyN), 22761 Hamburg, Germany; The Hamburg Centre for Ultrafast Imaging, 22761 Hamburg, Germany*

Hendrik Sannemüller − *Institute for Nanostructure and Solid State Physics, Center for Hybrid Nanostructures (CHyN), 22761 Hamburg, Germany*

Michael Jaruszewski − *Institute for Nanostructure and Solid State Physics, Center for Hybrid Nanostructures (CHyN), 22761 Hamburg, Germany*

Daniela Pfannkuche − *Institute for Theoretical Physics, University of Hamburg, 22607 Hamburg, Germany; The Hamburg Centre for Ultrafast Imaging, 22761 Hamburg, Germany*

Atsushi Urakawa − *Department of Chemical Engineering, Delft University of Technology, Delft 2629 HZ, The Netherlands;* orcid.org/0000-0001-7778-4008

Complete contact information is available at: https://pubs.acs.org/10.1021/acs.chemmater.2c03503

Notes

The authors declare no competing financial interest.

■ ACKNOWLEDGMENTS

This work was partially supported by the Cluster of Excellence "CUI: Advanced Imaging of Matter" of the Deutsche Forschungsgemeinschaft (DFG)−EXC 2056−project ID 390715994, by GRK 2536 NANOHYBRID of the Deutsche Forschungsgemeinschaft, and by the Bundesministerium für Bildung und Forschung (BMBF) via project LUCENT (Grant No. 05K19GU7). The authors thank Marvin Skiba for performing ICP-MS measurements, Sandra König for nitrogen physisorption measurements, Sarah-Alexandra Hussak for support in scanning electron microscopy imaging, Malte-Maximilian Schmidt for support in infrared spectroscopy measurements, Andrea Köppen and Stefan Werner for STEM/TEM imaging, Birgit Alpers for performing the CHN elemental analysis measurement, and Dr. Francesco Caddeo for support during the manuscript revision process, and the PHYSnet Computing Center for computing capacity. M.R. thanks Sönke Wengler-Rust for UV−vis training, Prof. Dr. Horst Weller for providing lab access, Qianqian Fang for technical support during the MMCLAB implementation, and Fabian Matter for sharing his expertise on the TiO_2 synthesis. M.J. thanks Martin Stieben and Bodo Krause-Kyora for technical support regarding calculations on the computing cluster.

■ REFERENCES

(1) Lewis, N. S.; Nocera, D. G. Powering the planet: Chemical challenges in solar energy utilization. *Proc. Natl. Acad. Sci. U.S.A.* **2006**, *103*, 15729−15735.

(2) Osterloh, F. E. Inorganic Materials as Catalysts for Photochemical Splitting of Water. *Chem. Mater.* **2008**, *20*, 35−54.

(3) Hambourger, M.; Moore, G. F.; Kramer, D. M.; Gust, D.; Moore, A. L.; Moore, T. A. Biology and technology for photochemical fuel production. *Chem. Soc. Rev.* **2009**, *38*, 25−35.

(4) Ma, Y.; Wang, X.; Jia, Y.; Chen, X.; Han, H.; Li, C. Titanium Dioxide-Based Nanomaterials for Photocatalytic Fuel Generations. *Chem. Rev.* **2014**, *114*, 9987−10043.

(5) Asahi, R.; Morikawa, T.; Irie, H.; Ohwaki, T. Nitrogen-Doped Titanium Dioxide as Visible-Light-Sensitive Photocatalyst: Designs, Developments, and Prospects. *Chem. Rev.* **2014**, *114*, 9824−9852.

(6) Chen, H. M.; Chen, C. K.; Liu, R.-S.; Zhang, L.; Zhang, J.; Wilkinson, D. P. Nano-architecture and material designs for water splitting photoelectrodes. *Chem. Soc. Rev.* **2012**, *41*, 5654−5671.

(7) Pan, J.; Liu, G.; Lu, G. Q.; Cheng, H.-M. On the True Photoreactivity Order of {001}, {010}, and {101} Facets of Anatase TiO_2 Crystals. *Angew. Chem., Int. Ed.* **2011**, *50*, 2133−2137.

(8) Chen, X.; Shen, S.; Guo, L.; Mao, S. S. Semiconductor-based Photocatalytic Hydrogen Generation. *Chem. Rev.* **2010**, *110*, 6503−6570.

(9) Rebber, M.; Willa, C.; Koziej, D. Organic−inorganic hybrids for CO_2 sensing, separation and conversion. *Nanoscale Horiz.* **2020**, *5*, 431−453.

(10) Ozin, G.; Kant, P. Will industrial-scale photocatalysis see the light of day? 2022 https://www.advancedsciencenews.com/will-industrial-scale-photocatalysis-see-the-light-of-day/. (accessed May 16, 2022).

(11) Zhakeyev, A.; Wang, P.; Zhang, L.; Shu, W.; Wang, H.; Xuan, J. Additive Manufacturing: Unlocking the Evolution of Energy Materials. *Adv. Sci.* **2017**, *4*, No. 1700187.

(12) Matter, F.; Niederberger, M. The Importance of the Macroscopic Geometry in Gas-Phase Photocatalysis. *Adv. Sci.* **2022**, *9*, No. 2105363.

(13) Wang, P.; Xuan, J.; Zhang, R.; Zhang, H.; Wang, Q.; Wang, H.; Liu, H.; Zhang, L. Hierarchically Structured Components: Design, Additive Manufacture, and Their Energy Applications. *Adv. Mater. Technol.* **2022**, *7*, No. 2100672.

(14) Zhou, H.; Li, X.; Fan, T.; Osterloh, F. E.; Ding, J.; Sabio, E. M.; Zhang, D.; Guo, Q. Artificial Inorganic Leafs for Efficient Photochemical Hydrogen Production Inspired by Natural Photosynthesis. *Adv. Mater.* **2010**, *22*, 951−956.

(15) DeLucia, E. H.; Nelson, K.; Vogelmann, T. C.; Smith, W. K. Contribution of intercellular reflectance to photosynthesis in shade leaves. *Plant, Cell Environ.* **1996**, *19*, 159−170.

(16) Shimoni, E.; Rav-Hon, O.; Ohad, I.; Brumfeld, V.; Reich, Z. Three-Dimensional Organization of Higher-Plant Chloroplast Thylakoid Membranes Revealed by Electron Tomography. *Plant Cell* **2005**, *17*, 2580−2586.

(17) Chameides, W. L.; Davis, D. D. The free radical chemistry of cloud droplets and its impact upon the composition of rain. *J. Geophys. Res.* **1982**, *87*, 4863−4877.

(18) Pieruschka, R.; Chavarría-Krauser, A.; Cloos, K.; Scharr, H.; Schurr, U.; Jahnke, S. Photosynthesis can be enhanced by lateral CO_2 diffusion inside leaves over distances of several millimeters. *New Phytol.* **2008**, *178*, 335−347.

(19) Parkhurst, D. F. Diffusion of CO_2 and other gases inside leaves. *New Phytol.* **1994**, *126*, 449−479.

(20) Li, X.; Fan, T.; Zhou, H.; Chow, S.-K.; Zhang, W.; Zhang, D.; Guo, Q.; Ogawa, H. Enhanced Light-Harvesting and Photocatalytic Properties in Morph-TiO_2 from Green-Leaf Biotemplates. *Adv. Funct. Mater.* **2009**, *19*, 45−56.

(21) Li, Y.; Fu, Z.-Y.; Su, B.-L. Hierarchically Structured Porous Materials for Energy Conversion and Storage. *Adv. Funct. Mater.* **2012**, *22*, 4634−4667.

(22) Fattakhova-Rohlfing, D.; Zaleska, A.; Bein, T. Three-Dimensional Titanium Dioxide Nanomaterials. *Chem. Rev.* **2014**, *114*, 9487−9558.

(23) Zhang, Q.; Chou, T. P.; Russo, B.; Jenekhe, S. A.; Cao, G. Polydisperse Aggregates of ZnO Nanocrystallites: A Method for Energy-Conversion-Efficiency Enhancement in Dye-Sensitized Solar Cells. *Adv. Funct. Mater.* **2008**, *18*, 1654−1660.

(24) Zhang, Q.; Chou, T. P.; Russo, B.; Jenekhe, S. A.; Cao, G. Aggregation of ZnO Nanocrystallites for High Conversion Efficiency in Dye-Sensitized Solar Cells. *Angew. Chem., Int. Ed.* **2008**, *47*, 2402−2406.

(25) Loh, J. Y. Y.; Mohan, A.; Flood, A. G.; Ozin, G. A.; Kherani, N. P. Waveguide photoreactor enhances solar fuels photon utilization towards maximal optoelectronic − photocatalytic synergy. *Nat. Commun.* **2021**, *12*, No. 402.

(26) He, Z.; Que, W. Surface scattering and reflecting: the effect on light absorption or photocatalytic activity of TiO_2 scattering microspheres. *Phys. Chem. Chem. Phys.* **2013**, *15*, 16768−16773.

(27) Luna, A. L.; Papadopoulos, S.; Kyburz, T.; Tervoort, E.; Novotny, L.; Niederberger, M. Insights into light and mass transport in nanoparticle-based aerogels: the advantages of monolithic 3D photocatalysts. *J. Mater. Chem. A* **2021**, *9*, 22380−22391.

(28) Wan, W.; Zhang, R.; Ma, M.; Zhou, Y. Monolithic aerogel photocatalysts: a review. *J. Mater. Chem. A* **2018**, *6*, 754−775.

(29) Phalippou, J.; Scherer, G. W.; Woignier, T.; Bourret, D.; Sempéré, R. Ultraporous materials with low permeability. *J. Non-Cryst. Solids* **1995**, *186*, 64−72.

(30) Kong, F. M.; LeMay, J. D.; Hulsey, S. S.; Alviso, C. T.; Pekala, R. W. Gas permeability of carbon aerogels. *J. Mater. Res.* **1993**, *8*, 3100−3105.

(31) Zeng, S. Q.; Hunt, A.; Greif, R. Transport properties of gas in silica aerogel. *J. Non-Cryst. Solids* **1995**, *186*, 264−270.

(32) Zhu, C.; Qi, Z.; Beck, V. A.; Luneau, M.; Lattimer, J.; Chen, W.; Worsley, M. A.; Ye, J.; Duoss, E. B.; Spadaccini, C. M.; Friend, C. M.; Biener, J. Toward digitally controlled catalyst architectures: Hierarchical nanoporous gold via 3D printing. *Sci. Adv.* **2018**, *4*, No. eaas9459.

(33) Friedmann, D.; Lee, A. F.; Wilson, K.; Jalili, R.; Caruso, R. A. Printing approaches to inorganic semiconductor photocatalyst fabrication. *J. Mater. Chem. A* **2019**, *7*, 10858−10878.

(34) Elkoro, A.; Soler, L.; Llorca, J.; Casanova, I. 3D printed microstructured Au/TiO_2 catalyst for hydrogen photoproduction. *Appl. Mater. Today* **2019**, *16*, 265−272.

(35) Chen, L.; Tang, X.; Xie, P.; Xu, J.; Chen, Z.; Cai, Z.; He, P.; Zhou, H.; Zhang, D.; Fan, T. 3D Printing of Artificial Leaf with Tunable Hierarchical Porosity for CO_2 Photoreduction. *Chem. Mater.* **2018**, *30*, 799−806.

(36) Zhao, L.; Yang, S.; Bhatia, B.; Strobach, E.; Wang, E. N. Modeling silica aerogel optical performance by determining its radiative properties. *AIP Adv.* **2016**, *6*, No. 025123.

(37) Jousten, K. *Handbuch Vakuumtechnik*; Springer Fachmedien Wiesbaden, 2018.

(38) Chiarello, G. L.; Ferri, D.; Selli, E. Effect of the CH_3OH/H_2O ratio on the mechanism of the gas-phase photocatalytic reforming of methanol on noble metal-modified TiO_2. *J. Catal.* **2011**, *280*, 168−177.

(39) Kotsokechagia, T.; Cellesi, F.; Thomas, A.; Niederberger, M.; Tirelli, N. Preparation of Ligand-Free TiO_2 (Anatase) Nanoparticles through a Nonaqueous Process and Their Surface Functionalization. *Langmuir* **2008**, *24*, 6988−6997.

(40) Rossi, L. M.; Fiorio, J. L.; Garcia, M. A. S.; Ferraz, C. P. The role and fate of capping ligands in colloidally prepared metal nanoparticle catalysts. *Dalton Trans.* **2018**, *47*, 5889−5915.

(41) Caravaca, A.; Daly, H.; Smith, M.; Mills, A.; Chansai, S.; Hardacre, C. Continuous flow gas phase photoreforming of methanol at elevated reaction temperatures sensitised by Pt/TiO_2. *React. Chem. Eng.* **2016**, *1*, 649−657.

(42) Walenta, C. A.; Courtois, C.; Kollmannsberger, S. L.; Eder, M.; Tschurl, M.; Heiz, U. Surface Species in Photocatalytic Methanol Reforming on Pt/TiO_2(110): Learning from Surface Science Experiments for Catalytically Relevant Conditions. *ACS Catal.* **2020**, *10*, 4080−4091.

(43) Phillips, K. R.; Jensen, S. C.; Baron, M.; Li, S.-C.; Friend, C. M. Sequential Photo-oxidation of Methanol to Methyl Formate on TiO_2(110). *J. Am. Chem. Soc.* **2013**, *135*, 574−577.

(44) Borges Ordoño, M.; Urakawa, A. Active Surface Species Ruling Product Selectivity in Photocatalytic CO_2 Reduction over Pt- or Co-Promoted TiO_2. *J. Phys. Chem. C* **2019**, *123*, 4140−4147.

(45) Bazzo, A.; Urakawa, A. Origin of Photocatalytic Activity in Continuous Gas Phase CO Reduction over Pt/TiO_2. *ChemSusChem* **2013**, *6*, 2095−2102.

(46) Joo, J. B.; Dillon, R.; Lee, I.; Yin, Y.; Bardeen, C. J.; Zaera, F. Promotion of atomic hydrogen recombination as an alternative to electron trapping for the role of metals in the photocatalytic production of H_2. *Proc. Natl. Acad. Sci. U.S.A.* **2014**, *111*, 7942−7947.

(47) Rolison, D. R.; Pietron, J. J.; Glaser, E. R.; Brintlinger, T. H.; Yesinowski, J. P.; DeSario, P. A.; Melinger, J. S.; Dunkelberger, A. D.; Miller, J. B.; Pitman, C. L.; Owrutsky, J. C.; Stroud, R. M.; Johannes, M. D. Power of Aerogel Platforms to Explore Mesoscale Transport in Catalysis. *ACS Appl. Mater. Interfaces* **2020**, *12*, 41277−41287.

(48) Rebber, M.; Trommler, M.; Lokteva, I.; Ehteram, S.; Schropp, A.; König, S.; Fröba, M.; Koziej, D. Additive-Free, Gelled Nanoinks as a 3D Printing Toolbox for Hierarchically Structured Bulk Aerogels. *Adv. Funct. Mater.* **2022**, *32*, No. 2112914.

(49) Luna, A. L.; Matter, F.; Schreck, M.; Wohlwend, J.; Tervoort, E.; Colbeau-Justin, C.; Niederberger, M. Monolithic metal-containing TiO_2 aerogels assembled from crystalline pre-formed nanoparticles as efficient photocatalysts for H_2 generation. *Appl. Catal., B* **2020**, *267*, No. 118660.

(50) Fang, Q.; Boas, D. A. In *Tetrahedral Mesh Generation from Volumetric Binary and Grayscale Images*, 2009 IEEE International Symposium on Biomedical Imaging: From Nano to Macro; IEEE: Boston, MA, USA, 2009; pp 1142−1145.

(51) Fang, Q. Mesh-based Monte Carlo method using fast ray-tracing in Plücker coordinates. *Biomed. Opt. Express* **2010**, *1*, 165−175.

(52) Liu, A.; Joe, B. Relationship between tetrahedron shape measures. *BIT Numer. Math.* **1994**, *34*, 268−287.

(53) Rebber, M.; Sannemüller, H.; Jaruszewski, M.; Pfannkuche, D.; Urakawa, A.; Koziej, D. Raw data for ″Light and mass transport computations guide the fabrication of 3D structured TiO_2 and Au/TiO_2 aerogel photocatalysts for efficient hydrogen production in the gas phase″. *zenodo* 2022, http://doi.org/10.5281/zenodo.7018488.